Physics of Fluids

RESEARCH ARTICLE | DECEMBER 12 2025

Data-driven reduced modeling of droplet shape evolution on inclined surfaces using the Onsager principle

Yujuan Chen ; Song Lu; Xianmin Xu

Physics of Fluids 37, 122126 (2025)
https://doi.org/10.1063/5.0302835

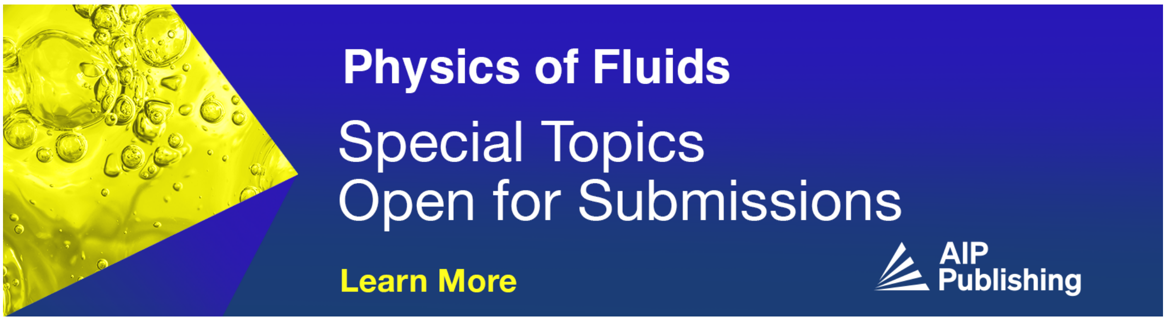

AIP Publishing

Physics of Fluids ARTICLE pubs.aip.org/aip/pof

Data-driven reduced modeling of droplet shape evolution on inclined surfaces using the Onsager principle

Cite as: Phys. Fluids **37**, 122126 (2025); doi: 10.1063/5.0302835
Submitted: 17 September 2025 · Accepted: 26 November 2025 ·
Published Online: 12 December 2025

Yujuan Chen,[1,2,a)] Song Lu,[3,4,b)] and Xianmin Xu[3,4,c)]

AFFILIATIONS

[1]College of Science, National University of Defense Technology, Changsha 410073, China
[2]State Key Laboratory of Space System Operation and Control, Changsha 410073, China
[3]State Key Laboratory of Mathematical Sciences, ICMSEC, NCMIS, Academy of Mathematics and Systems Sciences, Chinese Academy of Sciences, Beijing 100190, China
[4]School of Mathematical Sciences, University of Chinese Academy of Sciences, Beijing 100049, China

[a)]Electronic mail: chenyujuan23@nudt.edu.cn
[b)]Electronic mail: lusong@lsec.cc.ac.cn
[c)]Author to whom correspondence should be addressed: xmxu@lsec.cc.ac.cn

ABSTRACT

The motion of a droplet on an inclined surface involves complex interfacial dynamics in which contact line motion and shape evolution play a critical role. Classical continuum-based and reduced-order models can describe droplet behavior at small inclination angles but fail to capture essential morphological features—such as the sharp rear corner—observed experimentally at larger tilts. To address this limitation, we propose a data-driven reduced-order framework that integrates the Onsager variational principle with functional principal component analysis (FPCA). By extracting dominant basis functions directly from experimental droplet profiles, the method reduces computational cost while retaining physical interpretability. Numerical experiments show that the model accurately reproduces droplet morphologies across a broad range of inclination angles, correcting the unrealistic conical shapes predicted by previous formulations while maintaining the same degrees of freedom as the classical reduced model. More broadly, the approach provides a systematic strategy for embedding experimental data into variational modeling, offering new opportunities for predictive and efficient analysis of complex interfacial flows.

I. INTRODUCTION

The motion of liquid droplets on solid surfaces is a ubiquitous phenomenon encountered in both natural processes and engineering applications. Examples include raindrops sliding down glass windows, oil spreading on painted surfaces, and dew gliding on plant leaves. Extensive research has been conducted both theoretically and experimentally on this phenomenon in hydrodynamics.[1–7]

Theoretical analysis of sliding droplets presents significant challenges, primarily due to the complexities of contact line dynamics, including contact angle variations, singularities, and hysteresis.[8–10] Classical continuum-based models, such as the lubrication approximation[11,12] and Navier–Stokes solvers with appropriate boundary conditions,[13] are commonly used to describe droplet motion at macroscopic scales. However, capturing microscopic processes near the contact line often requires hybrid or multiscale techniques, which are computationally expensive and difficult to generalize.

When a millimeter-sized droplet slides down an inclined surface under partial wetting conditions, its shape undergoes distinct transitions with increasing tilt angle—from oval to cornered, cusp-like, and eventually rivulet-like forms.[4,14–16] In this regime, treating the droplet as a point mass becomes inadequate; instead, the influence of evolving droplet morphology must be explicitly accounted for. From a computational perspective, simulating this process remains highly demanding,[17–19] since droplet shape evolution strongly affects both trajectory and velocity distribution.

To overcome these challenges, Xu *et al.*[20] proposed a pioneering reduced-order model based on the Onsager variational principle.[21–25] Their framework achieved good agreement with experimental results[14] at small inclination angles. However, at larger tilts, the model failed to reproduce key morphological features, notably the experimentally observed sharp rear corner. Simply enriching the polynomial basis in such reduced formulations does not adequately resolve this limitation. While higher-order polynomial functions offer greater geometric flexibility, they also considerably increase computational complexity and tend to produce nonlinear systems with reduced numerical stability. This limitation highlights the need for a more systematic strategy to capture complex droplet shapes.

Beyond purely physics-based formulations, recent advances in data-driven modeling offer promising alternatives. Reduced-order approaches and neural-network-based frameworks have been introduced to complement classical models,[26–28] demonstrating that physical constraints can be effectively combined with data-driven insights to improve predictive accuracy and generalization. Motivated by these developments, the present study integrates experimental droplet profiles with the Onsager variational principle and employs functional principal component analysis (FPCA) for dimensionality reduction. By identifying dominant basis functions directly from data, the proposed framework reduces computational cost while retaining physical interpretability, thereby improving predictive accuracy at large inclination angles and yielding droplet morphologies in closer agreement with experimental observations.

It should be noted that the present study focuses on Newtonian fluid (silicone oil) droplets sliding on smooth inclined surfaces. Nevertheless, the proposed FPCA-enhanced variational framework is conceptually extensible to more complex interfacial systems. For instance, recent studies have reported distinct morphological and dynamical behaviors of non-Newtonian droplets, including shear-thinning and viscoelastic fluids, when sliding on hydrophobic or lubricated substrates.[29–31] Similarly, droplet deformation and motion under electric-field actuation have been widely investigated for both Newtonian and polymeric systems.[32–34] By appropriately incorporating experimental profile data or field-dependent parameters into the FPCA method, the present framework could be extended to describe such non-Newtonian or field-driven phenomena.

The remainder of this paper is organized as follows. Section II applies the Onsager variational principle to derive a modified model by combining the original model with the FPCA method for a droplet sliding on an inclined surface. Section III reports numerical results and their comparison with experimental data. Finally, Sec. IV summarizes the main findings and outlook.

II. THE MODEL DERIVED BY THE ONSAGER PRINCIPLE

This paper aims to study the behavior of a droplet sliding on an inclined surface at an angle α. A Cartesian coordinate system is established, where the z-axis is orthogonal to the base plane, the x-axis points in the direction of droplet descent, and the y-axis lies in the plane of the inclined surface. The shape of the droplet at time t is represented by the function $z = h(x, y, t)$, the side view profile of the droplet descent is represented by the function $z = H(x, t)$, and the contact line profile is represented by the function $y = Y(x, t)$. A schematic diagram of a droplet sliding down the inclined surface is shown in Fig. 1.

The shape of sliding liquid droplets has been the subject of research in both experimental and theoretical domains.[4,15,35] These studies indicate that the shape of the droplets can be approximated by the function $h(x, y, t)$,

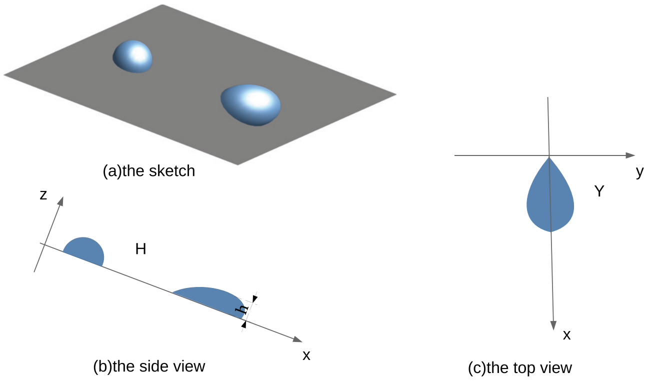

FIG. 1. Illustration of a droplet sliding down an inclined surface: (a) sketch of a droplet sliding on an inclined surface, (b) side view showing the side profile $H(x, t)$, and (c) top view showing the contact line profile $Y(x, t)$.

$$h(x, y, t) = H(x, t)\left[1 - \left(\frac{y}{Y(x, t)}\right)^2\right], \tag{1}$$

where $H(x, t)$ and $Y(x, t)$ are the functions to be determined. From Eq. (1), it can be observed that at a given x coordinate, the thickness h of the liquid droplet decreases parabolically with respect to y. The thickness of the droplet becomes zero at $y = Y(x, t)$ and at $y = 0$, the thickness of the droplet is $h = H(x, t)$. Therefore, this equation satisfies that the contact line of the droplet is given by the function $y = Y(x, t)$, and the side view of the droplet is specified by the function $z = H(x, t)$.

Assuming that the x coordinates of the rear and front parts of the contact line are denoted as a_1 and a_2, respectively, as shown in Fig. 2, the volume of the liquid droplet Ω can be calculated as follows:

$$\Omega = \int_{a_1}^{a_2} dx \int_{-Y}^{Y} dy h(x, y, t) . \tag{2}$$

Xu *et al.*[20] made further assumptions by considering the following form for $H(x, t)$ and $Y(x, t)$:

$$H(x, t) = (x - a_1(t))(a_2(t) - x)\ (a_3(t) + a_4(t)x), \tag{3}$$

$$Y(x, t) = (x - a_1(t))^{\frac{1}{2}}(a_2(t) - x)^{\frac{1}{2}}\ (a_5(t) + a_6(t)x). \tag{4}$$

Specifically, the parameters a_1 and a_2 denote the x-coordinates of the rear and front contact points, while a_3–a_6 represent deviations from the equilibrium profile. The fractional power-law dependence near $x = a_1$ and $x = a_2$ ensures rounded contours of the contact line of the droplet at both ends while allowing a cusp to emerge when $-a_5/a_6$ approaches a_1, consistent with experimental observations. They gave the free energy $A(a)$ and the energy dissipation function $\Phi(\dot{a}) = \frac{1}{2}\sum_{i,j}\zeta_{ij}\dot{a}_i\dot{a}_j$, and used Onsager principle $\frac{\partial\Phi}{\partial\dot{a}_i} + \frac{\partial A}{\partial a_i} = 0$ to obtain the time evolution equations for a_i as follows:

$$\sum_{j=1}^{6}\zeta_{ij}\dot{a}_j + \frac{\partial A}{\partial a_i} = 0, \tag{5}$$

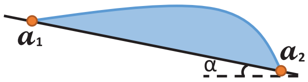

FIG. 2. Side view of a droplet sliding down.

where the coefficients ζ_{ij} are functions of $a = (a_1, a_2, \ldots, a_6)$. From Eq. (2), we know that Ω is a constant, which implies that only five out of the six parameters $a_i(t)$ are independent.

We aspire to improve the consistency between the model and experimental observations through the refinement of the assumptions about H and Y. A natural thought is to consider adding more polynomial basis functions to H and Y to enhance the flexibility and better fit the side profile and the contact line profile of the droplet, especially the sharp corner at the rear under large inclination angles. We initially explored this path by systematically increasing the number of basis functions.

For example, we considered higher-order polynomial forms such as

$$\begin{aligned} H_M(x,t) &= (x - a_1(t))(a_2(t) - x)P_M(x), \\ Y_N(x,t) &= (x - a_1(t))^{\frac{1}{2}}(a_2(t) - x)^{\frac{1}{2}}Q_N(x), \end{aligned} \tag{6}$$

where $P_M(x)$ and $Q_N(x)$ are polynomials of degrees M and N, respectively. Substituting these enhanced forms into the variational procedure yields a system of equations analogous to Eq. (5) but with more parameters.

However, our numerical experiments revealed a key limitation: merely increasing the number of basis functions in this *ad hoc* manner does not guarantee a better agreement with experimental droplet profiles. While the fitting flexibility increases, the model, without guidance from real data, often fails to converge to the physically correct morphology observed in experiments.

To address this, we pivot to a data-driven strategy that directly leverages experimental observations to inform the model. We utilize experimental images from Ref. 14, normalize the droplet length, and collect coordinate data points for the side and top views. We then employ the least squares method to fit the droplet contours to high-dimensional basis functions, obtaining an empirical representation of the side and contact line profiles,

$$H_5(x,t) = x(1-x)(a_3 + a_4x + a_5x^2 + a_6x^3 + a_7x^4 + a_8x^5), \tag{7}$$

$$Y_5(x,t) = x^{\frac{1}{2}}(1-x)^{\frac{1}{2}}\left(a_9 + a_{10}x + a_{11}x^2 + a_{12}x^3 + a_{13}x^4 + a_{14}x^5\right). \tag{8}$$

Here, x is the coordinate normalized to the interval [0, 1].

While these data-fitting step accurately captures the droplet profile, it significantly increases the number of parameters (a_3–a_{14}), leading to high computational complexity. To reduce the dimensionality while retaining the essential physical features encoded in the data, we employ FPCA.

FPCA is a technique that can be used to identify the main variation patterns from a set of function curves. It finds a set of orthogonal basis functions that are optimal in the sense that they capture the maximum variance in the data. This makes it ideally suited for our purpose: to distill the most important side profile and contact line profile characteristics from the high-dimensional fitted curves H_5 and Y_5 into a minimal set of basis functions, thereby dramatically reducing the number of degrees of freedom without sacrificing the accuracy of the profile representation. The specific steps of the FPCA algorithm applied to our problem are detailed in Algorithm 1.

ALGORITHM 1. Apply the FPCA algorithm for dimensional reduction of the basis functions.

Step 1. Given l sets of curve data points and a set of bases,

$$\begin{aligned} &\boldsymbol{S} = (\boldsymbol{s}^1, \boldsymbol{s}^2, \ldots, \boldsymbol{s}^l), \quad \Phi = (\phi_1(x), \phi_2(x), \ldots, \phi_m(x))^T, \\ &\boldsymbol{s}^{(i)} = \left((x_1^{(i)}, y_1^{(i)}), (x_2^{(i)}, y_2^{(i)}), \ldots, (x_n^{(i)}, y_n^{(i)})\right), \quad i = 1\ldots l. \end{aligned} \tag{9}$$

Step 2. Employ the least squares fitting method, and solve the following equation to obtain the coefficient matrix C:

$$\boldsymbol{C} = [\boldsymbol{C}_1, \boldsymbol{C}_2, \ldots, \boldsymbol{C}_l], \quad \min_{\boldsymbol{C}_i} \|\boldsymbol{Y}_i - \Psi_i \boldsymbol{C}_i\|_2. \tag{10}$$

where

$$\boldsymbol{Y}_i = \begin{bmatrix} y_1^{(i)} \\ y_2^{(i)} \\ \vdots \\ y_n^{(i)} \end{bmatrix}, \quad \boldsymbol{\Psi}_i = \begin{bmatrix} \phi_1(x_1^{(i)}) & \phi_2(x_1^{(i)}) & \ldots & \phi_m(x_1^{(i)}) \\ \phi_1(x_2^{(i)}) & \phi_2(x_2^{(i)}) & \ldots & \phi_m(x_2^{(i)}) \\ \vdots & \vdots & \ddots & \vdots \\ \phi_1(x_n^{(i)}) & \phi_2(x_n^{(i)}) & \ldots & \phi_m(x_n^{(i)}) \end{bmatrix}, \quad \boldsymbol{C}_i = \begin{bmatrix} c_1^{(i)} \\ c_2^{(i)} \\ \vdots \\ c_m^{(i)} \end{bmatrix}$$

Step 3. Calculate the mass matrix $\boldsymbol{M} = \int_0^1 \Phi\Phi^T dx$ and perform the Cholesky decomposition $\boldsymbol{M} = \boldsymbol{L}\boldsymbol{L}^T$ on it. Then, transform $\boldsymbol{A} := \boldsymbol{L}^T\boldsymbol{C}$.

Step 4. Perform the singular value decomposition (SVD) on the centralized $\boldsymbol{A}$.

$$\boldsymbol{A} = \boldsymbol{U}\Lambda\boldsymbol{V}^T, \tag{11}$$

where $\Lambda = \mathrm{diag}(\lambda_1, \lambda_2, \ldots, \lambda_q)$, $\lambda_1 \geq \lambda_2 \geq \cdots \geq \lambda_q > 0$, $\boldsymbol{U} = (\boldsymbol{u}_1, \boldsymbol{u}_2, \ldots, \boldsymbol{u}_q)$, $q = \mathrm{rank}(\boldsymbol{A})$.

Step 5. Choose an appropriate value for k such that $\sum_{i=1}^k \lambda_i^2 / \sum_{i=1}^q \lambda_i^2$ is greater than 0.8. Truncate $\boldsymbol{U}$ to obtain $\bar{\boldsymbol{U}} := (\boldsymbol{u}_1, \boldsymbol{u}_2, \ldots, \boldsymbol{u}_k)$.

Step 6. Left multiply $\bar{\boldsymbol{U}}$ by $\Phi^{\boldsymbol{T}}\boldsymbol{L}^{-T}$ to obtain the first k principal components.

$$\boldsymbol{B} := (\beta_1, \beta_2, \ldots, \beta_k) = \Phi^{\boldsymbol{T}}\boldsymbol{L}^{-T}\bar{\boldsymbol{U}}. \tag{12}$$

In this study, five sets of droplet profile data ($l = 5$) were extracted, respectively, for the side profiles (H) and contact line profiles (Y) from the experimental images reported by Le Grand *et al.*,[14] covering capillary numbers $Ca = 2.85 \times 10^{-3}$, 4.95×10^{-3}, 5.14×10^{-3}, 7.07×10^{-3}, and 7.19×10^{-3}. The dataset size for each profile type is constrained to five cases owing to the limited number of profiles that can be clearly digitizable in the original experiments. For the side and contact line profiles, we respectively choose the basis as

$$\Phi_H = \left(x(1-x), x^2(1-x), \ldots, x^6(1-x)\right)^T, \tag{13}$$

$$\Phi_Y = \left(x^{\frac{1}{2}}(1-x)^{\frac{1}{2}}, x^{\frac{3}{2}}(1-x)^{\frac{1}{2}}, \ldots, x^{\frac{11}{2}}(1-x)^{\frac{1}{2}}\right)^T. \tag{14}$$

To demonstrate the detailed implementation, the FPCA procedure is hereafter described using the side profile (H) as a representative example. The experimental contour is first represented as a discrete dataset $\boldsymbol{s}_H^{(i)} = \left\{\left(x_j^{(i)}, y_j^{(i)}\right)\right\}_{j=1}^{n}$, and the coefficient vector $\boldsymbol{C}_i$ corresponding to the polynomial basis Φ_H is obtained through least squares fitting. All coefficient vectors are then assembled into a matrix $\boldsymbol{C}_H = [\boldsymbol{C}_1, \boldsymbol{C}_2, \ldots, \boldsymbol{C}_l]$.

To preserve orthogonality in the functional space, a mass matrix is introduced as

$$\boldsymbol{M}_H = \int_0^1 \Phi_H(x)\Phi_H^T(x)\,dx, \tag{15}$$

which defines the weighted inner product in the $L^2([0,1])$ space spanned by the basis functions Φ_H. The Cholesky factorization $\boldsymbol{M}_H = \boldsymbol{L}_H\boldsymbol{L}_H^T$ is then applied to transform the weighted inner product into the standard Euclidean inner product through $\boldsymbol{A}_H = \boldsymbol{L}_H^T\boldsymbol{C}_H$. Finally, the transformed coefficient matrix $\boldsymbol{A}_H$ is centered by subtracting its mean row, and the SVD $\boldsymbol{A}_H = \boldsymbol{U}_H\Lambda_H\boldsymbol{V}_H^T$ is performed to extract the orthogonal principal components of droplet profiles.

The ith contribution rate are defined as

$$r_i^H = (\lambda_i^H)^2 \Big/ \sum_{i=1}^{q} (\lambda_i^H)^2, \tag{16}$$

where λ_i^H ($i = 1, \ldots, q$) are the non-zero singular values of $\boldsymbol{A}_H$ and $q = \mathrm{rank}(\boldsymbol{A}_H)$. The cumulative contribution ratio for the first k components is then given by $R_k^H = \sum_{i=1}^{k} r_i^H$, which is used to determine the effective dimensionality k required to capture the dominant deformation profiles. In FPCA, as well as in traditional PCA, it is standard practice to retain sufficient components to achieve a target level of cumulative explained variance. Typical thresholds reported in the literature range from 70% to 90%, depending on data characteristics and the desired balance between model accuracy and complexity.[36,37] Following this well-established convention, the present study adopts a cutoff of $R_k^H > 0.8$, thereby retaining the first k components that collectively account for more than 80% of the total variance. Finally, the corresponding functional principal components are reconstructed as

$$\boldsymbol{B}_H = \Phi_H^T\boldsymbol{L}_H^{-T}\bar{\boldsymbol{U}}_H, \tag{17}$$

where $\bar{\boldsymbol{U}}_H = [\boldsymbol{u}_1, \ldots, \boldsymbol{u}_k]$ contains the leading left singular vectors corresponding to the FPCA basis of the side profile.

As summarized in Table I, the first principal component accounts for more than 98% of the total variance for both the side and contact line profiles, indicating that a single FPCA basis ($k = 1$) is sufficient to capture the dominant profile variability while maintaining the same degrees of freedom as the classical reduced-order model. Therefore, we select these first principal components as our new, data-informed basis functions,

$$\beta_1^H = x(1-x)(215x^5 - 519x^4 + 472x^3 - 195x^2 + 44.9x - 12.2), \tag{18}$$

$$\beta_1^Y = x^{\frac{1}{2}}(1-x)^{\frac{1}{2}}(35.5x^5 - 95.6x^4 + 92.8x^3 - 34x^2 - 2.21x + 4.88). \tag{19}$$

TABLE I. The ith principal component contribution rates r_i^H and r_i^Y, $i = 1, \ldots, 5$ of side profiles (H) and contact line profiles (Y).

i	1	2	3	4	5
r_i^H	0.9833	1.5×10^{-2}	1.8×10^{-3}	2.2×10^{-4}	8.0×10^{-29}
r_i^Y	0.9956	3.7×10^{-3}	6.3×10^{-4}	4.3×10^{-5}	2.3×10^{-31}

The coefficients in Eqs. (18) and (19) originate from the first principal component obtained through FPCA of the experimental data after normalization to the interval [0, 1]. These coefficients are specific to the dataset and capture the structure of the droplet profiles, rather than representing universal constants.

We reconstruct droplet profiles by expressing the fitted curves in the FPCA-derived basis and projecting them back to the original space (see Fig. 3). The excellent agreement between the FPCA reconstructions and experimental profiles is quantified by the L_2 errors of 0.0025 (side profile) and 0.0031 (contact line profile). These results confirm that the reduced basis retains sufficient accuracy to represent droplet profiles while substantially lowering the dimensional complexity.

We now construct our final, optimized model by expressing H and Y using these data-driven basis functions. Restoring the original scaling with $a_1(t)$ and $a_2(t)$, we define

$$H_{new} = (x - a_1)(a_2 - x)[a_3 + a_4(215\bar{x}^5 - 519\bar{x}^4 + 472\bar{x}^3 - 195\bar{x}^2 + 44.9\bar{x} - 12.2)], \tag{20}$$

$$Y_{new} = (x - a_1)^{\frac{1}{2}}(a_2 - x)^{\frac{1}{2}}[a_5 + a_6(35.5\bar{x}^5 - 95.6\bar{x}^4 + 92.8\bar{x}^3 - 34\bar{x}^2 - 2.21\bar{x} + 4.88)], \tag{21}$$

where $\bar{x} = (x - a_1)/(a_2 - a_1)$ is the normalized coordinate.

Substituting H_{new} and Y_{new} into the Onsager principle yields the time evolution equation for the parameters a_i,

$$\sum_{j=1}^{6} \zeta_{ij}\dot{a}_j + \frac{\partial A}{\partial a_i} = 0. \tag{22}$$

Notably, the volume constraint in Eq. (2) ensures that only five of the six parameters are independent. The new model, presented in Eq. (22), preserves the same number of degrees of freedom as the original model by Xu *et al.*[20] in Eq. (5), but its dynamics are now guided by basis functions derived from experimental data, enabling a more physical and accurate representation of the droplet shape evolution.

III. NUMERICAL EXPERIMENTS

The physical experiment of a silicone oil droplet sliding down a glass plate coated with fluoropolymer was investigated by Le Grand *et al.*[14] Xu *et al.*[20] utilized the same parameters as the experimental

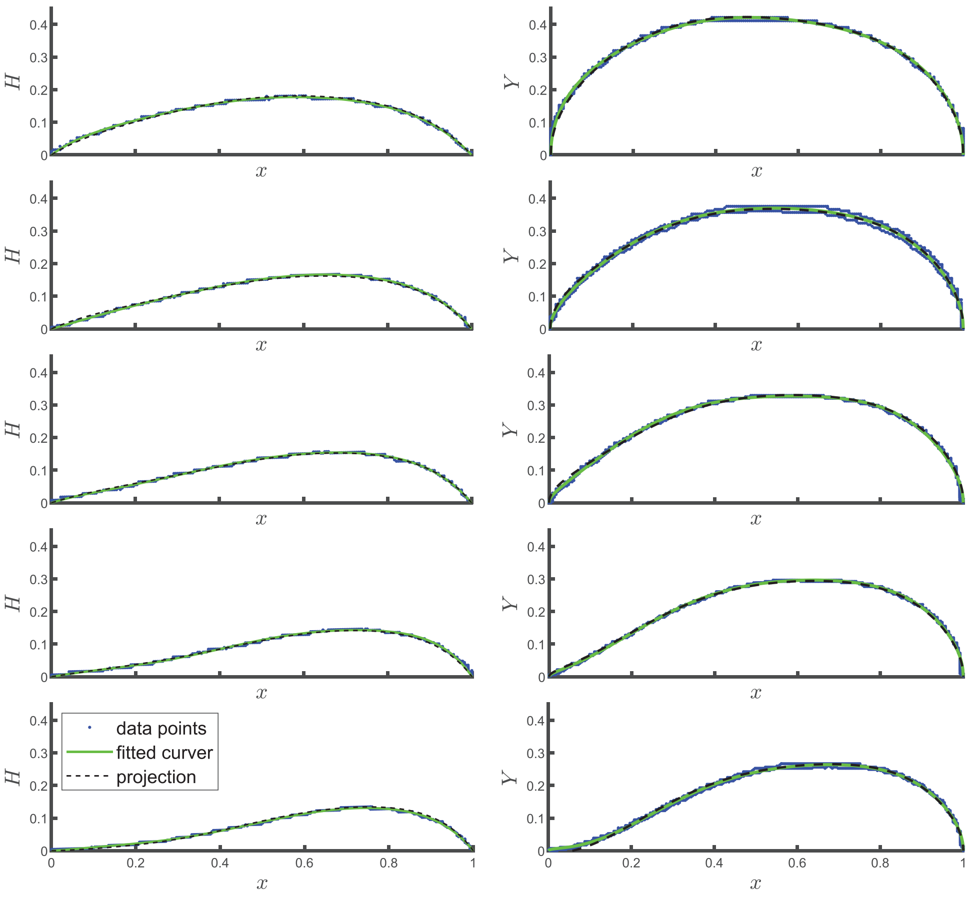

FIG. 3. Comparison between experimental droplet profiles and numerical reconstructions at different inclination angles (top to bottom, increasing α). Blue dots represent experimental data points, green lines denote least squares fits, and black dashed lines show reconstructions obtained by projecting FPCA-reduced basis functions back to the original space. Left: side profile (corresponding to H) and right: contact line profile (corresponding to Y).

study conducted by Le Grand *et al.*[14] in their numerical computations. These parameters include the viscosity $\eta = 104\,\text{cP}$, density $\rho = 964\,\text{kg/m}^3$, surface tension $\gamma = 20.9\,\text{mN/m}$, droplet volume $\Omega = 6.3\,\text{mm}^3$, and the equilibrium contact angle $\theta_e = 53°$ equals to the advancing contact angle reported in Ref. 14. It can be easily estimated that the Reynolds number $Re \ll 1$, indicating that the inertial effects can be neglected.

Figure 4 illustrates the scaling relation between the capillary number $Ca = \eta U/\gamma$ and the Bond number $Bo_\alpha = V^{2/3}(\rho g/\gamma)\sin\alpha$, where U is the sliding velocity, and α the inclination angle. Data corresponding to $\alpha = 5°$, $15°$, $25°$, $35°$, and $45°$ collapse onto a nearly linear trend, in agreement with experimental observations.[14] This result verifies that the reduced-order model preserves the correct force balance governing droplet motion and thereby maintains physical consistency across a wide range of inclination angles.

Figure 5 illustrates that at $\alpha = 45°$, the proposed model yields a droplet contour with a rounded apex and rear curvature that more closely resemble experimental observations, in contrast to the conical shape predicted by the original formulation. This improvement becomes even more evident when compared directly with experimental profiles[14] in Fig. 6. Quantitatively, the average L_2 error relative to the experimental profile decreases from 0.1290 for the classical Onsager-based model to 0.0206 for the FPCA-enhanced model, indicating improved agreement with the experiments. The enhanced accuracy arises from incorporating FPCA-based basis functions, which capture complex profile variations while preserving the same degrees of freedom as the original Onsager model.[20] By reducing dimensional complexity without sacrificing fidelity, the refined model achieves both

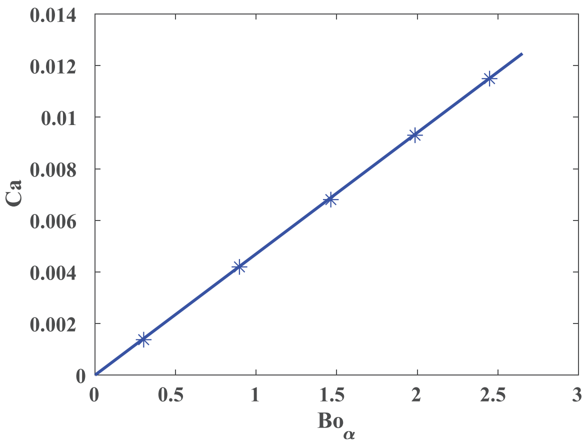

FIG. 4. Relationship between the capillary number $Ca = \eta U/\gamma$ and the Bond number $Bo_\alpha = V^{2/3}(\rho g/\gamma)\sin\alpha$ for sliding droplets at different inclination angles (5°, 15°, 25°, 35°, and 45°).

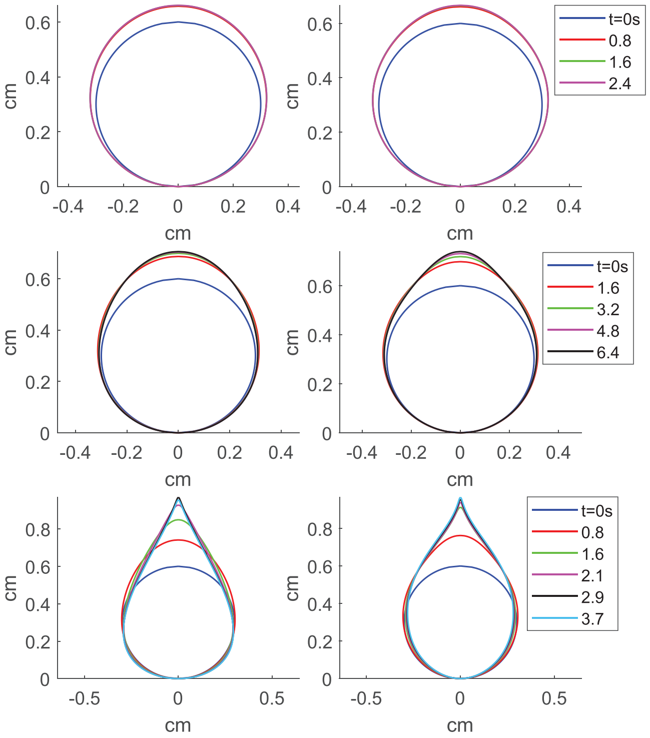

FIG. 5. Contact line profile comparison of droplets predicted by the classical Onsager-based model Eq. (5) (left: corresponding to Y) and the proposed FPCA-enhanced model Eq. (22) (right: corresponding to Y_{new}) at inclination angles of 15°, 25°, and 45° (top to bottom).

computational efficiency and improved predictive power for droplet morphology.

Compared with the polynomial enrichment approach, the superior performance of the FPCA-enhanced model stems from its data-driven construction. While higher-order polynomial bases increase the geometric flexibility of the representation, they also considerably increase computational complexity and tend to produce nonlinear systems with reduced numerical stability. In contrast, the FPCA basis functions are directly extracted from experimental contour profiles, inherently encoding nonlinear geometric features. Through these data-driven embeddings, the FPCA-enhanced model captures the dominant deformation modes that govern droplet evolution, enabling accurate reconstruction of both the side and contact line profiles. This explains why the FPCA-enhanced model achieves both lower L_2 errors and qualitatively more realistic profiles compared with polynomial enrichment under the same number of degrees of freedom.

To further assess the generalizability of the proposed model beyond the reference case, a parameter sensitivity analysis was conducted. As shown in Fig. 7, the evolution of droplet profiles was simulated for different viscosities ($\eta = 204\,\text{cP}$ and $\eta = 1040\,\text{cP}$) at the inclination angle of 45°. The droplets exhibit deformation and sliding behaviors qualitatively similar to the reference case with $\eta = 104\,\text{cP}$ (as shown in Fig. 6). However, the time required to reach steady state increases significantly with viscosity. When $\eta = 204\,\text{cP}$, the droplet takes longer to reach a steady state, and for $\eta = 1040\,\text{cP}$, the sliding process becomes substantially slower owing to enhanced viscous dissipation. These observations are consistent with the experimental findings of Le Grand *et al.*[14]

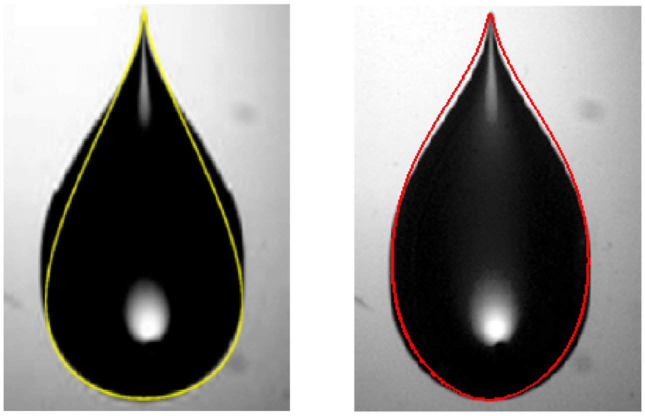

FIG. 6. Comparison of numerical results and experimental results[14] [Fig. 4(e), reproduced with permission] for droplet contact line profile at $Ca = 7.19 \times 10^{-3}$ by the classical Onsager-based model Eq. (5) (left: corresponding to Y, average L_2 error 0.1290) and the proposed FPCA-enhanced model Eq. (22) (right: corresponding to Y_{new}, average L_2 error 0.0206). Reproduced with permission from Le Grand *et al.* J. Fluid Mech. **541**, 293–315 (2005). Copyright 2005 Cambridge University Press.

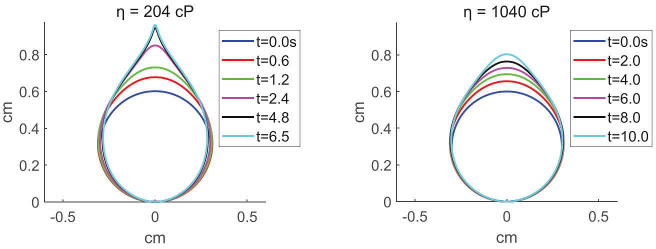

FIG. 7. Comparison of droplet evolution at an inclination angle of 45° for different viscosities: $\eta = 204\,\text{cP}$ and $\eta = 1040\,\text{cP}$. Both cases exhibit similar deformation and sliding behavior as the reference case ($\eta = 104\,\text{cP}$), while higher viscosity results in slower motion and longer time before reaching the steady state.

IV. SUMMARY

This work proposed a data-driven reduced-order model for the shape evolution of droplets sliding on inclined surfaces. By combining experimental contour profiles with the Onsager variational principle, the model incorporated physical constraints while leveraging data to refine basis functions. Functional principal component analysis (FPCA) was employed to extract dominant modes, thereby reducing computational complexity without sacrificing accuracy.

Numerical results demonstrated that the proposed framework significantly improves upon the classical reduced model,[20] particularly at larger inclination angles. Unlike earlier formulations that predicted unrealistic conical shapes, the new model successfully reproduces the curved apex and sharper rear corner observed in experiments. Moreover, the capillary—bond number relationship obtained numerically was consistent with physical principles, further validating the approach.

The methodological contribution of this work lies in showing how experimental data can be systematically integrated into variational modeling through FPCA-based reduction. This not only enhances predictive accuracy but also ensures physical interpretability. Although the model demonstrates strong predictive performance, its accuracy relies on the availability and representativeness of experimental contour data used for FPCA training. The current implementation is limited to the steady sliding of Newtonian droplets (silicone oil) under moderate inclination angles. Future directions include extending the framework to three-dimensional droplets with anisotropic contact angles, incorporating heterogeneous surface geometries, exploring transport phenomena in microfluidic environments, and exploring synergies with physics-informed neural networks for broader generalization.

ACKNOWLEDGMENTS

This work was partially supported by the National Key R&D Program of China (Grant No. 2024YFA1012502), the Natural Science Foundation of Hunan Province (Grant No. 2025JJ60045), the National Natural Science Foundation of China (Grant Nos. 12371415 and 12461160275), and the Natural Science Foundation of Beijing Municipality (Grant No. Z240001).

AUTHOR DECLARATIONS

Conflict of Interest

The authors have no conflicts to disclose.

Author Contributions

Yujuan Chen: Conceptualization (equal); Investigation (equal); Writing – original draft (equal); Writing – review & editing (equal). **Song Lu:** Data curation (equal). **Xianmin Xu:** Conceptualization (equal); Methodology (equal); Writing – review & editing (equal).

DATA AVAILABILITY

The data that support the findings of this study are available from the corresponding author upon reasonable request.

REFERENCES

[1] P. G. de Gennes, "Wetting: Statics and dynamics," Rev. Mod. Phys. **57**, 827–863 (1985).

[2] P. G. de Gennes, F. Brochard-Wyart, and D. Quéré, *Capillarity and Wetting Phenomena: Drops, Bubbles, Pearls, Waves* (Springer, 2004).

[3] D. Bonn, J. Eggers, J. Indekeu, J. Meunier, and E. Rolley, "Wetting and spreading," Rev. Mod. Phys. **81**, 739–805 (2009).

[4] T. Podgorski, J. M. Flesselles, and L. Limat, "Corners, cusps, and pearls in running drops," Phys. Rev. Lett. **87**(3), 036102 (2001).

[5] D. Quéré, "Wetting and roughness," Annu. Rev. Mater. Res. **38**(1), 71–99 (2008).

[6] J. H. Snoeijer and B. Andreotti, "Moving contact lines: Scales, regimes, and dynamical transitions," Annu. Rev. Fluid Mech. **45**(1), 269–292 (2013).

[7] B. Li, L. Fan, J. Bai, H. Xiang, and Y. Yuan, "Water-droplet impact and sliding behaviors on slippery surfaces with various weber numbers and surface inclinations," Coatings **13**(2), 264 (2023).

[8] C. Huh and L. E. Scriven, "Hydrodynamic model of steady movement of a solid/liquid/fluid contact line," J. Colloid Interface Sci. **35**, 85–101 (1971).

[9] O. V. Voinov, "Hydrodynamics of wetting," Fluid Dyn. **11**(5), 714–721 (1977).

[10] A. Mohammad Karim, "A review of physics of moving contact line dynamics models and its applications in interfacial science," J. Appl. Phys. **132**(8), 080701 (2022).

[11] A. Oron, S. H. Davis, and S. G. Bankoff, "Long-scale evolution of thin liquid films," Rev. Mod. Phys. **69**, 931–980 (1997).

[12] R. V. Craster and O. K. Matar, "Dynamics and stability of thin liquid films," Rev. Mod. Phys. **81**(3), 1131–1198 (2009).

[13] W. Ren, "Boundary conditions for the moving contact line problem," Phys. Fluids **19**(2), 646754 (2007).

[14] N. Le Grand, A. Daerr, and L. Limat, "Shape and motion of drops sliding down an inclined plane," J. Fluid Mech. **541**, 293–315 (2005).

[15] J. H. Snoeijer, E. Rio, N. Le Grand, and L. Limat, "Self-similar flow and contact line geometry at the rear of cornered drops," Phys. Fluids **17**(7), 946607 (2005).

[16] J. H. Snoeijer, L. Grand-Piteira, L. Limat, H. A. Stone, and J. Eggers, "Cornered drops and rivulets," Phys. Fluids **19**(4), 042104 (2007).

[17] Y. Sui, H. Ding, and P. Spelt, "Numerical simulations of flows with moving contact lines," Annu. Rev. Fluid Mech. **46**(1), 97–119 (2014).

[18] H. Ding and P. Spelt, "Wetting condition in diffuse interface simulations of contact line motion," Phys. Rev. E **75**(4), 046708 (2007).

[19] L. Sigalotti, J. Klapp, and E. Sira, *Computational and Experimental Fluid Mechanics with Applications to Physics, Engineering and the Environment* (Springer Science & Business Media, 2014).

[20] X. Xu, Y. Di, and M. Doi, "Variational method for liquids moving on a substrate," Phys. Fluids **28**(8), 087101 (2016).

[21] M. Doi, "Onsager principle as a tool for approximation," Chin. Phys. B **24**(2), 020505 (2015).

[22] M. Doi, *Soft Matter Physics* (Oxford University Press, 2013).

[23] M. Doi, "Onsager's variational principle in soft matter," J. Phys.:Condens. Matter **23**(28), 284118 (2011).

[24] L. Onsager, "Reciprocal relations in irreversible processes. I," Phys. Rev. **37**(4), 405–426 (1931).

[25] L. Onsager, "Reciprocal relations in irreversible processes. II," Phys. Rev. **38**(12), 2265–2279 (1931).

[26] H. Yu, X. Tian, Weinan. E, and Q. Li, "ONSAGERNET: Learning stable and interpretable dynamics using a generalized Onsager principle," Phys. Rev. Fluids **6**(11), 114402 (2021).

[27] S. L. Brunton, B. R. Noack, and P. Koumoutsakos, "Machine learning for fluid mechanics," Annu. Rev. Fluid Mech. **52**(1), 477–508 (2020).

[28] M. Raissi, P. Perdikaris, and G. E. Karniadakis, "Physics-informed neural networks: A deep learning framework for solving forward and inverse problems involving nonlinear partial differential equations," J. Comput. Phys. **378**, 686–707 (2019).

[29] S. A. Haider and A. Raj, "Static behavior and classification of shear-thinning droplets on inclined hydrophobic substrates," Phys. Fluids **37**(10), 102102 (2025).

[30] P. Sartori, D. Ferraro, M. Dassie, A. Meggiolaro, D. Filippi, A. Zaltron, M. Pierno, and G. Mistura, "Oscillatory motion of viscoelastic drops on slippery lubricated surfaces," Commun. Phys. **5**(1), 81 (2022).

[31] S. Varagnolo, G. Mistura, M. Pierno, and M. Sbragaglia, "Sliding droplets of xanthan solutions: A joint experimental and numerical study," Eur. Phys. J. E **38**(11), 126 (2015).

[32] J. S. Eow, M. Ghadiri, and A. Sharif, "Experimental studies of deformation and break-up of aqueous drops in high electric fields," Colloids Surf. A **225**(1), 193–210 (2003).

[33] J. Liu and S. Liu, "Dynamics behaviors of droplet on hydrophobic surfaces driven by electric field," Micromachines **10**(11), 778 (2019).

[34] X. Huang, X. Luo, Y. Han, W. Li, Y. Lai, and L. Teng, "Deformation and breakup of water droplets containing polymer under a dc electric field," AIChE J. **68**(10), e17786 (2022).

[35] L. Limat and H. A. Stone, "Three-dimensional lubrication model of a contact line corner singularity," Europhys. Lett. **65**, 365–371 (2004).

[36] I. T. Jolliffe, *Principal Component Analysis* (Springer, 2002).

[37] I. T. Jolliffe and J. Cadima, "Principal component analysis: A review and recent developments," Philos. Trans. R. Soc., A **374**, 20150202 (2016).